JACS
JOURNAL OF THE AMERICAN CHEMICAL SOCIETY
Article
pubs.acs.org/JACS

Dynamic Multibody Protein Interactions Suggest Versatile Pathways for Copper Trafficking

Aaron M. Keller,[†] Jaime J. Benítez,[†] Derek Klarin,[§,†] Linghao Zhong,[‡] Matthew Goldfogel,[⊥,†] Feng Yang,[†] Tai-Yen Chen,[†] and Peng Chen*[,†]

[†]Department of Chemistry and Chemical Biology, Cornell University, Ithaca, New York 14853, United States
[‡]Department of Chemistry, Pennsylvania State University, Mont Alto, Pennsylvania 17237, United States

Supporting Information

ABSTRACT: As part of intracellular copper trafficking pathways, the human copper chaperone Hah1 delivers Cu^+ to the Wilson's Disease Protein (WDP) via weak and dynamic protein−protein interactions. WDP contains six homologous metal binding domains (MBDs) connected by flexible linkers, and these MBDs all can receive Cu^+ from Hah1. The functional roles of the MBD multiplicity in Cu^+ trafficking are not well understood. Building on our previous study of the dynamic interactions between Hah1 and the isolated fourth MBD of WDP, here we study how Hah1 interacts with MBD34, a double-domain WDP construct, using single-molecule fluorescence resonance energy transfer (smFRET) combined with vesicle trapping. By alternating the positions of the smFRET donor and acceptor, we systematically probed Hah1−MBD3, Hah1−MBD4, and MBD3−MBD4 interaction dynamics within the multidomain system. We found that the two interconverting interaction geometries were conserved in both intermolecular Hah1−MBD and intramolecular MBD−MBD interactions. The Hah1−MBD interactions within MBD34 are stabilized by an order of magnitude relative to the isolated single-MBDs, and thermodynamic and kinetic evidence suggest that Hah1 can interact with both MBDs simultaneously. The enhanced interaction stability of Hah1 with the multi-MBD system, the dynamic intramolecular MBD−MBD interactions, and the ability of Hah1 to interact with multiple MBDs simultaneously suggest an efficient and versatile mechanism for the Hah1-to-WDP pathway to transport Cu^+.

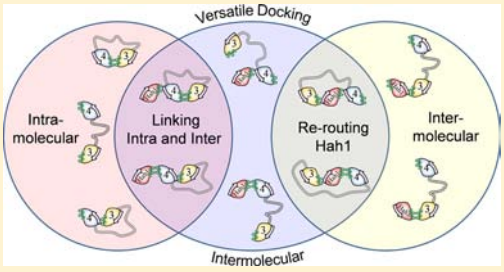

1. INTRODUCTION

Copper is an essential cofactor for many enzymes, but it must be safely transported and regulated in the cell to avoid harmful effects such as oxidative damage.[1] In humans, the copper chaperone, Hah1, specifically delivers Cu^+ via weak and dynamic protein interactions to two homologous P_{1B}-type ATPases: the Wilson's Disease Protein (WDP) and the Menkes' Disease Protein (MNK).[2] Under normal conditions both WDP and MNK reside in the trans-Golgi network and use ATP hydrolysis to drive Cu^+ translocation from the cytosol into the Golgi for later incorporation into various copper enzymes.[3] Under elevated Cu^+ stress, they relocalize for the export of Cu^+ from the cell.[4] Genetic defects in WDP and MNK result in copper toxicity and deficiency disorders respectively.[5]

Both WDP and MNK have six cytosolic N-terminal metal binding domains (MBDs, numbered 1−6 starting from the N-terminus) connected by flexible linkers of various lengths. Interestingly, the number of MBDs varies between one and six with higher organisms generally having more MBDs.[6] The catalytic core of WDP/MNK contains eight transmembrane helices that constitute the Cu^+ pump, an ATP-binding domain, and an actuator domain involved in the regulation of Cu^+ translocation.[4c,7]

The individual WDP/MNK MBDs and Hah1 are all homologous, each having a $\beta\alpha\beta\beta\alpha\beta$ protein fold and a CXXC Cu^+-binding motif.[8] They can all bind Cu^+ with a similar high affinity ($\sim 10^{18}$ M^{-1}), which was also observed for homologous proteins.[9] Under a shallow thermodynamic gradient, Hah1 can transfer Cu^+ to each MBD with similar efficiency.[9a,10] The Cu^+ transfer is mediated by weak and dynamic protein interactions, $K_D \sim \mu M$, and involves metal-bridging of the CXXC motifs of the two proteins.[2a,c,d,11]

Despite the many similarities among the MBDs, various differences exist. These differences include electrostatic potentials, locations within the N-terminal tail, ability to reorient with regard to the adjacent linkers, and complex formation with other MBDs or Hah1.[12] A combination of yeast two-hybrid assays[2c,13] and NMR studies[10,12b,14] have shown that, in general, Hah1 preferentially interacts with MBDs 1−4 over MBDs 5−6. Further, yeast complementation[15] and cellular imaging studies[16] showed that only MBDs 5−6 were essential for maintaining WDP function. It is also possible that the multiple MBDs function to regulate the Cu^+-translocation activity[4c,7,17] or relocalization of WDP/MNK for Cu^+-efflux[4c,16,18] via large-scale conformational changes in the cytoplasmic tail.[12a,d,14a,19]

Both intermolecular Hah1−MBD interactions and intramolecular MBD−MBD interactions are vital to WDP/MNK's function. Characterizing and understanding these weak and

Received: February 25, 2012
Published: May 11, 2012

   dx.doi.org/10.1021/ja3018835 | J. Am. Chem. Soc. 2012, 134, 8934−8943

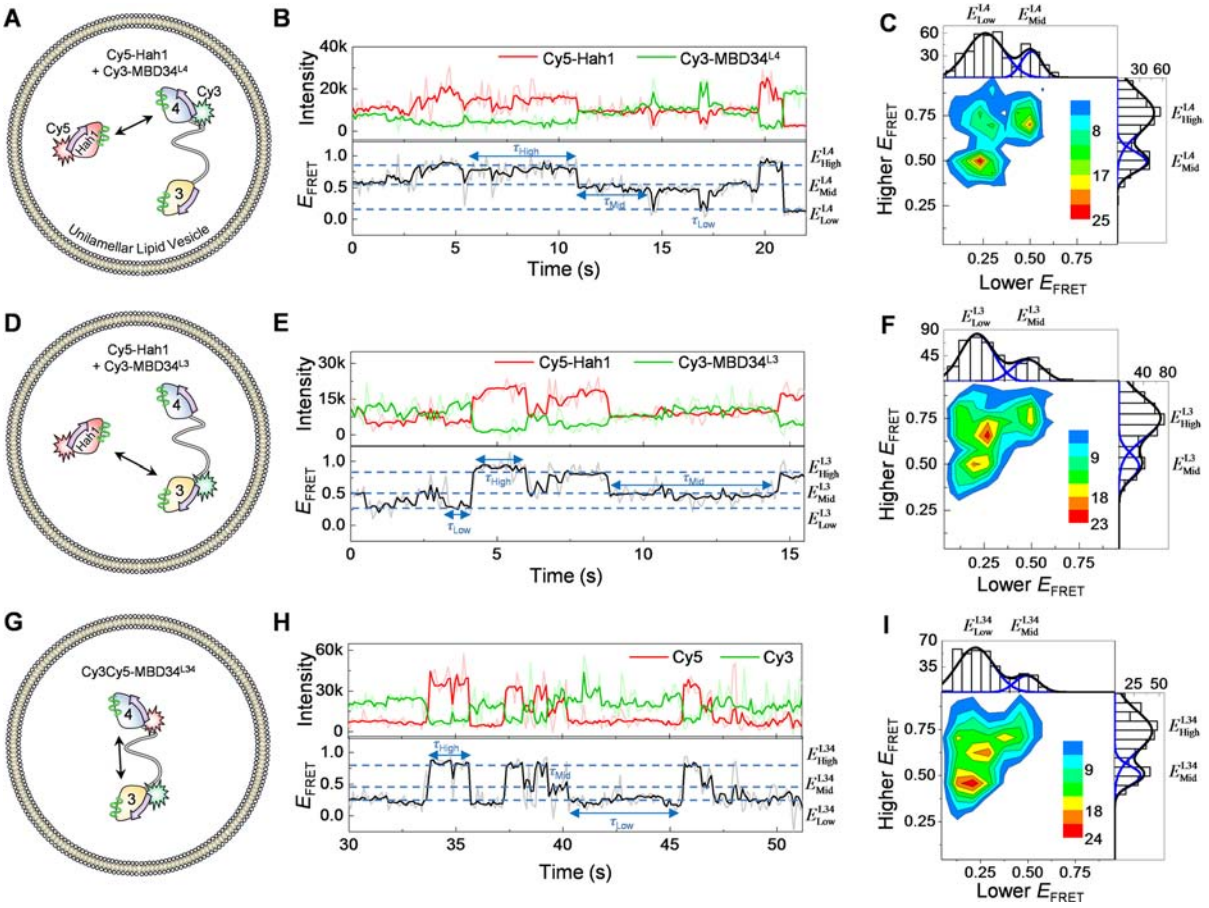

Figure 1. (A) Cy5−Hah1 + Cy3−MBD34^{L4} labeling scheme to probe Hah1−MBD4 interactions, (B) corresponding smFRET trajectory, and (C) two-dimensional (2-D) histogram of the average lower vs average higher E_{FRET} state for 226 pairs. (D) Cy5−Hah1 + Cy3−MBD34^{L3} labeling scheme to probe Hah1−MBD3 interactions, (E) corresponding smFRET trajectory, and (F) 2-D E_{FRET} histogram for 285 pairs. (G) Cy3Cy5−MBD34^{L34} labeling scheme to probe MBD3−MBD4 interactions, (H) corresponding smFRET trajectory, and (I) 2-D E_{FRET} histogram for 248 molecules. In all trajectories, the light colors show the original fluorescence intensities and corresponding E_{FRET} while the darker colors represent data subjected to nonlinear forward−backward filtering (section S9 [SI]). For each 2-D histogram, three populations are observed, corresponding to E_{Low}−E_{Mid}, E_{Low}−E_{High}, and E_{Mid}−E_{High} combinations. The 1-D projections of the histograms and their Gaussian resolution allow for the determination of the center E_{FRET} values.

dynamic protein interactions remains an important, yet challenging, task. Surface plasmon resonance studies have been used to study the kinetics of these interactions,[20] but nonspecific protein−surface interactions may perturb the kinetics. NMR,[10,12b,14,21] X-ray crystallography,[11a,22] protein docking,[11b] and molecular dynamic (MD) simulations[11d,12c,d,23] have provided detailed structural information on the interaction interfaces, but can only provide estimates on the interaction thermodynamics and kinetics.

To compliment these studies while overcoming some of their limitations, we use single-molecule fluorescence resonance energy transfer (smFRET)[24] in combination with vesicle trapping[25] to quantify weak and dynamic Hah1−MBD and MBD−MBD interactions. By labeling Hah1 and the MBDs with a smFRET donor−acceptor pair, we can monitor the interaction dynamics of a single pair in real time. This eliminates the need for synchronization and allows us to observe interaction intermediates that are otherwise masked in ensemble-averaged measurements. The proteins are trapped within a surface-immobilized ∼100-nm diameter unilamellar lipid vesicle, which maintains an effective protein concentration of ∼μM, needed for studying weak interactions ($K_D \approx \mu$M), while also eliminating nonspecific protein−surface interactions. This approach also eliminates homodimeric interactions between two proteins of the same type, which are unavoidable in ensemble measurements.

We have previously used this approach to study interactions between Hah1 and the isolated fourth MBD of WDP, denoted MBD4^{SD} (SD: "single domain"), both in the absence and presence of Cu^+.[26] We found that Hah1 interacts with MBD4^{SD} in two geometries, which can interconvert dynamically. We hypothesized that these multiple interaction geometries increase the probability of forming a complex for Cu^+ transfer, and that the two geometries may allow for Hah1 interaction with multiple MBDs simultaneously. Both interaction geometries are stabilized in the presence of 1 equiv of Cu^+, and destabilized under excess Cu^+ loading.

Here we seek to understand Hah1−WDP interactions in the context of WDP's multi-MBD structure, using a WDP construct containing its third and fourth MBDs, MBD34. We have systematically probed Hah1−MBD3, Hah1−MBD4, and MBD3−MBD4 interactions using a series of FRET labeling schemes. Note that we use the terms "MBD3" and "MBD4" to refer to the respective MBDs within the multidomain MBD34 construct. To probe whether Hah1−MBD interactions are influenced by the presence of additional MBDs, we compare

dx.doi.org/10.1021/ja3018835 | J. Am. Chem. Soc. 2012, 134, 8934−8943

Hah1−MBD4^{SD} vs Hah1−MBD4 interactions. To probe whether Hah1 interacts preferentially with certain MBDs, we compare Hah1−MBD4 vs Hah1−MBD3. To understand intramolecular-interdomain interactions between MBDs and how they are coupled to intermolecular interactions with Hah1, we have studied the MBD3−MBD4 interactions both in the absence and presence of Hah1. To probe what role multiple MBDs play during the trafficking of Cu^+, we have studied the Cu^+-dependence of Hah1−MBD4 interactions. Finally, we propose a mechanism for the Hah1−multi-MBD interactions and describe its functional significance for Cu^+ trafficking.

2. EXPERIMENTAL SECTION

The Supporting Information (SI) presents the experimental methods (sections S1−9 [SI]), including the design of Hah1 and MBD34 constructs; protein expression, purification, and characterization; protein labeling with FRET probes, and subsequent purification and characterization; Cu^+ removal; vesicle trapping, smFRET measurements, data analysis, and control experiments.

3. RESULTS AND ANALYSIS

3.1. FRET Labeling Schemes for Dissecting Protein Interactions. We used three donor−acceptor (Cy3−Cy5) FRET labeling schemes to dissect the inter- and intramolecular interactions among Hah1 and the two MBDs of MBD34. To directly observe Hah1−MBD4 interactions, we labeled Hah1 at its C-terminus (i.e., C69) with Cy5, and MBD4 at its C-terminus (i.e., C206) with Cy3 (Figure 1A); we refer to this MBD34 construct as "Cy3−MBD34^{L4}," where L4 denotes that the label is on MBD4. To directly observe Hah1−MBD3 interactions, we labeled MBD3 at its C-terminus (i.e., C95) with Cy3 (Figure 1D); we refer to this MBD34 construct as "Cy3−MBD34^{L3}." To observe intramolecular-interdomain MBD3−MBD4 interactions within MBD34, we labeled these two domains at their respective C-terminals (i.e., C95 and C206) with the Cy3−Cy5 pair (Figure 1G); the Cy3 or Cy5 can be attached to either of the two cysteines; we refer to this double-labeled MBD34 construct as "Cy3Cy5−MBD34^{L34}." This double labeling also generated MBD34 molecules that contain two Cy3 or two Cy5; these could be easily differentiated in our smFRET experiments and were excluded in our data analysis (section S9 [SI]). In all MBD34 constructs, the cysteines in the CXXC motif of MBD3 were mutated to alanines to remove MBD3's Cu^+-binding capability, so Cu^+-transfer could only occur between Hah1 and MBD4.

3.2. Observation of Dynamic Protein−Protein Interactions in the Absence of Cu^+. By trapping two protein molecules labeled with the Cy3−Cy5 pair or a single protein labeled with this pair within an immobilized vesicle and measuring their smFRET, we first studied the dynamic interactions between Hah1 and MBD34 and between the two domains of MBD34 in the absence of Cu^+.

For all labeling schemes we observed anticorrelated Cy3−Cy5 donor−acceptor fluorescence intensity fluctuations, reporting the dynamic intermolecular Hah1−MBD (Figure 1B, E) and intramolecular MBD3−MBD4 interactions (Figure 1H). In each case, three interconverting E_{FRET} states are apparent, at E_{FRET} ~0.2, ~0.5, and ~0.8. We refer to these respective states as E^{L4}_{Low}, E^{L4}_{Mid}, and E^{L4}_{High} for the Cy5−Hah1 + Cy3−MBD34^{L4} labeling scheme; E^{L3}_{Low}, E^{L3}_{Mid}, and E^{L3}_{High} for the Cy5−Hah1 + Cy3−MBD34^{L3} labeling scheme; and E^{L34}_{Low}, E^{L34}_{Mid}, and E^{L34}_{High} for the Cy3Cy5−MBD34^{L34} labeling scheme.

Because many smFRET trajectories showed only two E_{FRET} states before the Cy3 or Cy5 was photobleached, we pooled data from a few hundred interacting pairs for each labeling scheme and examined the 2-dimensional (2-D) histogram of the average lower (either E_{Low} or E_{Mid}) vs higher (either E_{Mid} or E_{High}) E_{FRET} values (Figure 1C, F, I). Three distinct populations are clear in each 2-D histogram, whose Gaussian-resolved peak values are E^{L4}_{Low} = 0.26 ± 0.01, E^{L4}_{Mid} = 0.50 ± 0.01, and E^{L4}_{High} = 0.77 ± 0.01 for Cy5−Hah1 + Cy3−MBD34^{L4}; E^{L3}_{Low} = 0.21 ± 0.01, E^{L3}_{Mid} = 0.49 ± 0.02, and E^{L3}_{High} = 0.76 ± 0.01 for Cy5−Hah1 + Cy3−MBD34^{L3}; and E^{L34}_{Low} = 0.22 ± 0.01, E^{L34}_{Mid} = 0.50 ± 0.02, and E^{L34}_{High} = 0.75 ± 0.01 for Cy3Cy5−MBD34^{L34}.

The large values of E_{Mid} and E_{High} indicate the formation of intermolecular Hah1−MBD or intramolecular MBD3−MBD4 interaction complexes, as the Cy3 and Cy5 labels should be within a few nm from each other. The significant difference between E_{Mid} and E_{High} indicates that these two E_{FRET} states correspond to two protein interaction geometries, similar to that observed in our previous study of Hah1 interacting with the single-domain construct, MBD4^{SD}.[26a] The similarity in the E_{Mid} and E_{High} values across the three labeling schemes indicates that the two interaction geometries are conserved between Hah1−MBD4, Hah1−MBD3, and MBD3−MBD4 interactions, consistent with Hah1 and all WDP MBDs being homologous.

For the two labeling schemes that probe intermolecular Hah1−MBD interactions, the E^{L4}_{Low} and E^{L3}_{Low} states represent the case where the proteins are far apart, yet their E_{FRET} values are higher than that of a completely dissociated state, E_{Dissoc} = 0.15 ± 0.01, which was independently determined in control experiments with vesicles containing free Cy3 and Cy5 and in our previous study of Hah1−MBD4^{SD} interactions.[25d,26a] Therefore, besides the dissociated species, the E^{L4}_{Low} state must contain Cy5−Hah1 interactions with the unlabeled MBD3 in Cy3−MBD34^{L4}, and the E^{L3}_{Low} state must contain Cy5−Hah1 interactions with the unlabeled MBD4 in Cy3−MBD34^{L3}.

For Cy3Cy5−MBD34^{L34}, E^{L34}_{Low} corresponds to the state where MBD3 and MBD4 are separate with their linker in a highly flexible, extended conformation (denoted as MBD34$_{ext}$); this conformation was observed in MBD34's NMR structures (Figure S1,SI).[21d] The E_{FRET} value of this extended confirmation should be smaller than those of intramolecular-interdomain complexes, but higher than that of the dissociated state E_{Dissoc} of intermolecular interactions, as observed. It is worth noting that E^{L34}_{Low} also approximates the E_{FRET} value when Cy5−Hah1 interacts with the respective unlabeled domain of Cy3−MBD34^{L4} or Cy3−MBD34^{L3} (i.e., $E^{L34}_{Low} \approx E^{L3}_{Low} \approx E^{L4}_{Low}$).

Combining all above results, we have studied how Hah1 interacts with each MBD within the double-domain WDP construct, MBD34, and how the two domains in MBD34 interact with each other in the absence of Cu^+. Hah1 can interact with each MBD forming two different complexes. Correlating with our previous work on Hah1 interaction with MBD4^{SD},[26] the results show that Hah1 can interact with MBD4 in two geometries in both the single-domain MBD4^{SD} and the double-domain MBD34 constructs. For MBD3, our results represent the first direct observation of any complex formation with Hah1. Moreover, we observed two MBD3−MBD4 interactions with geometries similar to Hah1−MBD interactions; this is the first direct observation of intramolecular-interdomain complexes between MBD3 and MBD4. It appears that the two interaction geometries are conserved for any pair between Hah1, MBD3, and MBD4, which are all homologous to each other. This conservation in interaction geometries

indicates that Hah1, MBD3, and MBD4 use similar protein surface patches for their interactions.

3.3. Stabilities of Hah1−MBD34 Intermolecular Interactions in the Absence of Cu$^+$. B and C of Figure 2 show

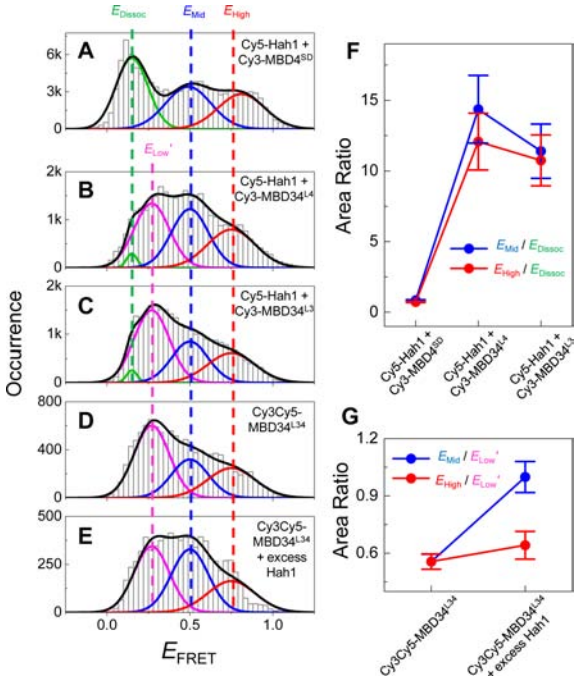

Figure 2. Compiled E_{FRET} distributions (bin size = 0.03) and corresponding Gaussian fits for (A) Cy5−Hah1 + Cy3−MBD4^{SD}, (B) Cy5−Hah1 + Cy3−MBD34^{L4}, (C) Cy5−Hah1 + Cy3−MBD34^{L3}, (D) Cy3Cy5−MBD34^{L34}, and (E) Cy3Cy5−MBD34^{L34} with excess Hah1. The E_{FRET} distributions were fitted globally by sharing the center values and widths of each E_{FRET} state. (F) The area ratios of E_{Mid} and E_{High} states with respect to E_{Dissoc} for Cy5−Hah1 + Cy3−MBD4^{SD}, Cy5−Hah1 + Cy3−MBD34^{L4}, and Cy5−Hah1 + Cy3−MBD34^{L3} determined from A−C. (G) The area ratios of E_{Mid} and E_{High} with respect to E_{Low}′ for Cy3Cy5−MBD34^{L34} and Cy3Cy5−MBD34^{L34} with excess Hah1 determined from D−E.

the E_{FRET} distributions from hundreds of smFRET trajectories of Cy5−Hah1 interacting with Cy3−MBD34^{L4} or Cy3−MBD34^{L3}, along with that of Cy5−Hah1 interacting with Cy3−MBD4^{SD} that we reported previously (Figure 2A).[25d,26a] These E_{FRET} distributions can be Gaussian-resolved to individual E_{FRET} states; the relative areas of the resolved peaks reflect the relative stabilities of chemical species associated with the E_{FRET} states.

For Cy5−Hah1 + Cy3−MBD4^{SD}, as determined previously,[25d,26a] the E_{FRET} distribution contains three peaks (Figure 2A): $E_{Dissoc} \approx 0.15$, $E_{Mid} \approx 0.50$, and $E_{High} \approx 0.81$, corresponding to the dissociated state and the two Hah1−MBD4^{SD} interaction complexes, respectively.

For Cy5−Hah1 + Cy3−MBD34^{L4}, we used four Gaussian peaks to resolve the E_{FRET} distribution (Figure 2B). Two of them are centered at $E^{L4}_{Mid} \approx 0.50$ and $E^{L4}_{High} \approx 0.75$, as resolved in Figure 1C, which correspond to the complexes between Hah1 and MBD4. For the other two, one accounts for the dissociated state (E_{Dissoc}), which is centered at ∼0.15 as resolved from the Cy5−Hah1 + Cy3−MBD4^{SD} E_{FRET} distribution (Figure 2A) and appears as a shoulder in Figure 2B; the other accounts for the state where Cy5−Hah1 forms complexes with the unlabeled MBD3 in Cy3−MBD34^{L4} ($E'^{L4}_{Low} \approx 0.27$) as discussed in section 3.2, and its center was floated in Gaussian-resolving the E_{FRET} distribution. Note, E_{Dissoc} and E'^{L4}_{Low} are unresolved within the E^{L4}_{Low} state in Figure 1C.

Similarly, for Cy5−Hah1 + Cy3−MBD34^{L3}, we used four Gaussian peaks to resolve the E_{FRET} distribution, centered at $E_{Dissoc} \approx 0.15$, $E'^{L3}_{Low} \sim 0.27$, $E^{L3}_{Mid} \approx 0.50$, and $E^{L3}_{High} \approx 0.75$, corresponding to the dissociated state, the state where Hah1 interacts with the unlabeled MBD4, and the two states where Hah1 complexes with MBD3, respectively (Figure 2C). The center positions and widths of these peaks were shared with those in the E_{FRET} distribution of Cy5−Hah1 + Cy3−MBD34^{L4} in Figure 2B; this is a valid approximation as the center positions determined through the 2-D E_{FRET} analyses are the same within experimental error for Cy5−Hah1 + Cy3−MBD34^{L4} and Cy5−Hah1 + Cy3−MBD34^{L3} (C and F of Figure 1). Furthermore, because E_{Dissoc} represents the same dissociated state for both Cy5−Hah1 + Cy3−MBD34^{L4} and Cy5−Hah1 + Cy3−MBD34^{L3} labeling schemes, the relative peak area of the E_{Dissoc} state is shared between B and C of Figure 2.

The deconvolution of E_{Low}′ from E_{Dissoc} in these E_{FRET} distributions allows us to account for Cy5−Hah1's interactions with the unlabeled domain within Cy3−MBD34^{L4} or Cy3−MBD34^{L3}, so that we can quantify the stability of the Hah1−MBD interactions relative to the dissociated state E_{Dissoc}, given by the peak area ratios in the E_{FRET} distributions. In both Cy5−Hah1 + Cy3−MBD34^{L4} and Cy5−Hah1 + Cy3−MBD34^{L3} labeling schemes, the E_{Mid}/E_{Dissoc} and E_{High}/E_{Dissoc} area ratios are comparable (Figure 2F), indicating that Hah1−MBD3 and Hah1−MBD4 interactions have similar stabilities. However, compared with Hah1−MBD4^{SD} interactions, Hah1 interactions with MBD4 and MBD3 within MBD34 are both more stable by an order of magnitude, reflected by the increase in E_{Mid}/E_{Dissoc} and E_{High}/E_{Dissoc} area ratios (Figure 2F). This increased stability indicates that there are concerted actions between the two MBDs (and perhaps the linker region) in MBD34 for interacting with Hah1.

The similar stability of Hah1−MBD3 and Hah1−MBD4 interactions suggests that Hah1 does not have significant preference for interacting with one MBD over the other within the double-domain construct MBD34. This is contrary to previous NMR experiments, which only detected Hah1 complex formation with MBD4 and not MBD3 (in the presence of Cu$^+$),[10,21d] but is in agreement with the yeast two-hybrid assay, which also detected Hah1−MBD3 interactions.[2c] The comparable complex formation of Hah1 with these MBDs observed here may explain why Cu$^+$-loaded Hah1 can metalate both MBD3 and MBD4 fully.[9a,10,21d]

The area percentages (χ) of the E_{FRET} states in the E_{FRET} distributions can be used to analyze the population percentages of all complexes. From the Cy5−Hah1 + Cy3−MBD34^{L4} E_{FRET} distribution (Figure 2B), the total population percentage of Hah1 in complexes with MBD4 is $\chi^{L4}_{Mid} + \chi^{L4}_{High} = 62 \pm 4\%$. From the Cy5−Hah1 + Cy3−MBD34^{L3} E_{FRET} distribution (Figure 2C), the total population percentage of Hah1 in complexes with MBD3 is $\chi^{L3}_{Mid} + \chi^{L3}_{High} = 52 \pm 9\%$. Interestingly, the total population percentage of Hah1 in complexes with either MBD3 or MBD4 would then sum to greater than unity ($114 \pm 10\%$). This suggests there must be overlap ($>14 \pm 10\%$) between the population of Hah1 in complexes with MBD3 and that of Hah1 in complexes with MBD4. In other words, there must be a population in which Hah1 is in close proximity with MBD4 and MBD3 *simultaneously*, e.g., forming 3-body interactions.

dx.doi.org/10.1021/ja3018835 | J. Am. Chem. Soc. 2012, 134, 8934−8943

In the Cy5−Hah1 + Cy3−MBD34^{L4} E_{FRET} distribution (Figure 2B), the E'^{L4}_{Low} state represents Hah1 interactions with the unlabeled MBD3 in the MBD34$_{ext}$ conformation (as any interactions involving MBD4 are contained in E^{L4}_{Mid} or E^{L4}_{High}). Its population percentage, χ'^{L4}_{Low} = 35 ± 4%, is significantly less than the population percentage of all Hah1 complexes with MBD3 determined from the Cy5−Hah1 + Cy3−MBD34^{L3} E_{FRET} distribution ($\chi^{L3}_{Mid} + \chi^{L3}_{High}$ = 52 ± 9%, Figure 2C); the difference between the above percentages again indicates that there is overlap (17 ± 10%) between the apparent Hah1−MBD3 and Hah1−MBD4 complexes.

Similarly, in the Cy5−Hah1 + Cy3−MBD34^{L3} E_{FRET} distribution (Figure 2C), the E'^{L3}_{Low} state represents Hah1 interactions with the unlabeled MBD4 in the MBD34$_{ext}$ conformation. Its population percentage, χ'^{L3}_{Low} = 46 ± 9%, is less than the population percentage of all Hah1 complexes with MBD4 determined from the Cy5−Hah1 + Cy3−MBD34^{L4} E_{FRET} distribution ($\chi^{L4}_{Mid} + \chi^{L4}_{High}$ = 62 ± 4%, Figure 2B). In agreement with the analysis above, the difference (16 ± 8%) again reflects a population overlap in the apparent Hah1−MBD3 and Hah1−MBD4 complexes.

To summarize, the population analysis of Cy5−Hah1 interacting with Cy3−MBD4^{SD}, Cy3−MBD34^{L4}, and Cy3−MBD34^{L3} demonstrates that Hah1 interactions with MBDs within the double-domain construct MBD34 are significantly more stable than with the isolated MBD4^{SD}. Moreover, Hah1−MBD3 and Hah1−MBD4 interactions have similar stability; and Hah1 can be in close proximity to MBD3 and MBD4 *simultaneously,* with an occurrence of ∼16%.

3.4. Time Scales of Intermolecular Hah1−MBD34 Interactions in the Absence of Cu$^+$. From the smFRET trajectories (B, E, and H of Figure 1), we can quantify the stochastic dwell times (τ_{Low}, τ_{Mid}, and τ_{High}) of the three E_{FRET} states (E_{Low}, E_{Mid}, and E_{High}). The distributions of these dwell times all follow single-exponential decay approximately: $f(\tau) = N \exp(-\tau/\bar{\tau})$, where $\bar{\tau}$ is a time constant and N is a scaling factor (Figure 3 and S3). $\bar{\tau}$ is also equivalent to the average of the respective dwell time and represents the apparent lifetime of that E_{FRET} state. Table 1 summarizes the apparent lifetimes ($\bar{\tau}_{Low}$, $\bar{\tau}_{Mid}$, and $\bar{\tau}_{High}$) of each E_{FRET} state for each labeling scheme.

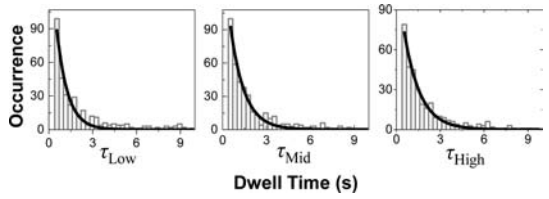

Figure 3. Distributions of the dwell time τ_{Low}, τ_{Mid}, and τ_{High} from E_{FRET} trajectories of Cy5−Hah1 + Cy3−MBD34^{L4}. Bin size = 0.3 s. Solid lines are fits with a single-exponential decay function, $f(\tau) = N \exp(-\tau/\bar{\tau})$. Here $\bar{\tau}$ is the decay time constant, which also represents the average dwell time. N is a scaling factor. This analysis was performed for the dwell times from E_{FRET} trajectories for all labeling schemes (section S11 [SI]). $\bar{\tau}_{Low}$, $\bar{\tau}_{Mid}$, and $\bar{\tau}_{High}$ represent the apparent lifetime of respective states (Table 1).

For the Cy5−Hah1 + Cy3−MBD34^{L4} and Cy5−Hah1 + Cy3−MBD34^{L3} labeling schemes, $\bar{\tau}_{Mid}$ and $\bar{\tau}_{High}$ represent the apparent lifetimes of the interaction complexes between Hah1 and MBD4 or between Hah1 and MBD3, respectively. Unfortunately, $\bar{\tau}_{Low}$ is not the lifetime of the dissociated state, as the E_{Low} state in the smFRET trajectories contains contributions from both the dissociated state (E_{Dissoc}) and the complexes in which Cy5−Hah1 interacts with the unlabeled domain in Cy3−MBD34^{L4} or Cy3−MBD34^{L3} (i.e., E_{Low}′), as discussed in sections 3.2 and 3.3. In both labeling schemes, the population of E_{Low}′ state is much higher than that of E_{Dissoc}, shown by the resolved E_{FRET} distributions (Figure 2B, C). Therefore, $\bar{\tau}_{Low}$ predominantly represents the apparent lifetime of E_{Low}′ for these two labeling schemes.

Table 1. Average Dwell Time (seconds) of each E_{FRET} State

experiment	$\bar{\tau}_{Low}$	$\bar{\tau}_{Mid}$	$\bar{\tau}_{High}$
apo Cy5−Hah1 + Cy3−MBD4^{SD}	0.97 ± 0.07	0.88 ± 0.05	0.67 ± 0.04
apo Cy5−Hah1 + Cy3−MBD34^{L4}	0.77 ± 0.06	0.95 ± 0.05	1.09 ± 0.06
+ 1 equiv of Cu$^+$	0.83 ± 0.07	0.85 ± 0.05	0.95 ± 0.05
+ 2 equiv of Cu$^+$	0.62 ± 0.04	0.44 ± 0.02	0.53 ± 0.03
+ 4 equiv of Cu$^+$	0.67 ± 0.04	0.43 ± 0.02	0.48 ± 0.02
apo Cy5−Hah1 + Cy3−MBD34^{L3}	0.89 ± 0.06	0.80 ± 0.04	0.69 ± 0.03
Cy3Cy5−MBD34^{L34}	0.59 ± 0.03	0.64 ± 0.03	0.61 ± 0.03
+ excess Hah1	0.48 ± 0.02	0.38 ± 0.01	0.34 ± 0.01

Comparing the apparent lifetimes of Hah1−MBD4 and Hah1−MBD4^{SD} complexes (from Cy5−Hah1 interacting with Cy3−MBD34^{L4} or Cy3−MBD4^{SD}), $\bar{\tau}_{Mid}$ is similar in both cases (∼0.9 s), whereas $\bar{\tau}_{High}$ is slightly longer for Hah1−MBD4 (∼1.1 s) vs Hah1−MBD4^{SD} (∼0.7 s) (Table 1). These comparable or slightly longer lifetimes of the Hah1−MBD4 interaction complexes cannot account fully for the order-of-magnitude increase in complex stability observed in the E_{FRET} distributions (Figure 2B vs Figure 2A, and Figure 2F). Therefore, there must be a significant decrease in the lifetime of the dissociated state for Hah1 interacting with the double-domain construct MBD34. This decrease in the lifetime of the dissociated state has also been proposed by van Dongen et al. to rationalize the increased affinity of Hah1 interacting with a four-domain WDP construct (MBDs 1−4) as compared with single-isolated MBDs, arising from the presence of multiple binding sites for Hah1.[13] Unfortunately, we could not determine the lifetime of the dissociated state due to its minor contribution to the experimental $\bar{\tau}_{Low}$.

Comparing the apparent lifetimes of Hah1−MBD4 and Hah1−MBD3 complexes (from Cy5−Hah1 interacting with Cy3−MBD34^{L4} or Cy3−MBD4^{L3}), $\bar{\tau}_{Mid}$ and $\bar{\tau}_{High}$ are slightly longer for Hah1−MBD4 complexes, but are still in similar magnitude (∼1 s, Table 1). This is consistent with the similar stabilities of Hah1−MBD4 and Hah1−MBD3 interactions, given by the area ratios of their respective E_{FRET} states (Figure 2F). Their $\bar{\tau}_{Low}$'s are also similar, and mainly reflect the lifetimes for Cy5−Hah1 interactions with the respective unlabeled domain within Cy3−MBD34^{L4} or Cy3−MBD34^{L3}.

In short, here we have examined the apparent lifetimes of the E_{FRET} states for Cy5−Hah1 interacting with Cy3−MBD4^{SD}, Cy3−MBD34^{L4}, or Cy3−MBD34^{L3} to assess the kinetic aspect of the trends in complex stability for Hah1−MBD4^{SD}, Hah1−MBD4, and Hah1−MBD3 interactions. Comparing Hah1−MBD4 vs Hah1−MBD3 interactions, the apparent lifetimes of the protein complexes are similar, consistent with their similar apparent stabilities. However, the apparent lifetimes of their complexes are also similar to those of Hah1−MBD4^{SD} interactions; therefore, the increased complex stabilities in Hah1's interactions with MBD34 likely come from an increase

dx.doi.org/10.1021/ja3018835 | J. Am. Chem. Soc. 2012, 134, 8934−8943

in the rate of protein association, rather than decrease in protein dissociation.

3.5. Stabilities and Kinetics of Intramolecular−Interdomain Interactions within MBD34. Using Cy3Cy5−MBD34^{L34}, we observed intramolecular interactions between MBD3 and MBD4 (section 3.2). Besides the extended conformation, MBD34$_{ext}$ (i.e, E^{L34}_{Low}), two intramolecular−interdomain complexes are clear (i.e., E^{L34}_{Mid} and E^{L34}_{High}), which interconvert dynamically (Figure 1H and I). Scheme 1 presents the simplest kinetic scheme describing these intramolecular−interdomain interactions within MBD34.

Scheme 1. Kinetic Mechanism of the Intramolecular−Interdomain Interactions between MBD3 and MBD4. Rate Constants: $k_1 = 0.9 \pm 0.1\ s^{-1}$, $k_{-1} = 0.88 \pm 0.09\ s^{-1}$, $k_2 = 0.79 \pm 0.05\ s^{-1}$, $k_{-2} = 0.76 \pm 0.08\ s^{-1}$, $k_3 = 0.69 \pm 0.03\ s^{-1}$, and $k_{-3} = 0.87 \pm 0.04\ s^{-1}$; Equilibrium Constants: $K_1^{34} = 1.0 \pm 0.2$, $K_2^{34} = 1.0 \pm 0.1$, and $K_{int}^{34} = 0.79 \pm 0.05$

$$K_1^{34} = \frac{[{}^1\mathrm{MBD34}]}{[\mathrm{MBD34_{ext}}]} = \frac{k_1}{k_{-1}}$$

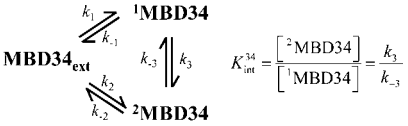

$$K_{int}^{34} = \frac{[{}^2\mathrm{MBD34}]}{[{}^1\mathrm{MBD34}]} = \frac{k_3}{k_{-3}}$$

$$K_2^{34} = \frac{[{}^2\mathrm{MBD34}]}{[\mathrm{MBD34_{ext}}]} = \frac{k_2}{k_{-2}}$$

Accordingly, we used three Gaussian peaks to resolve the E_{FRET} distribution of Cy3Cy5−MBD34^{L34} (Figure 2D). They are centered at $E'^{L34}_{Low} \approx 0.27$, $E^{L34}_{Mid} \approx 0.50$, and $E^{L34}_{High} \approx 0.75$, corresponding to the extended conformation, MBD34$_{ext}$, and the two intramolecular-interdomain complexes, denoted as ^{1}MBD34 and ^{2}MBD34, respectively. The center value and width of the E'^{L34}_{Low} peak were shared with E'^{L3}_{Low} and E'^{L4}_{Low} in B and C of Figure 2 because the observed E_{FRET} for MBD34$_{ext}$ in the Cy3Cy5−MBD34^{L34} labeling scheme should be similar to Cy5−Hah1 interacting with the unlabeled domain in Cy3−MBD34^{L4} or Cy3−MBD34^{L3}. The center values and widths of E^{L34}_{Mid} and E^{L34}_{High} were shared with the other distributions as well because the two interaction geometries between any pair of Hah1, MBD3, and MBD4 appear conserved as noted previously (section 3.2). Relative to the extended conformation, MBD34$_{ext}$, the equilibrium stability constants of ^{1}MBD34 ($K_1^{34} = 0.6 \pm 0.2$) and ^{2}MBD34 ($K_2^{34} = 0.6 \pm 0.2$) can be obtained from the peak area ratios in the Cy3Cy5−MBD34^{L34} E_{FRET} distribution (Figure 2D and Scheme 1). These two intramolecular complexes are approximately equal in stability.

The kinetics of the intramolecular−interdomain interactions can be quantified from the E_{FRET} state lifetimes ($\bar{\tau}_{Low}$, $\bar{\tau}_{Mid}$, and $\bar{\tau}_{High}$) for Cy3Cy5−MBD34^{L34} using the kinetic mechanism in Scheme 1 (section S12 [SI]).[25d,26b] The intramolecular−interdomain association rate constants (k_1 and k_2), the dissociation rate constants (k_{-1} and k_{-2}), and the interconversion rate constants (k_3 and k_{-3}) all occur in similar time scales, $\sim 1\ s^{-1}$. The rate constants also give the equilibrium constants, $K_1^{34} = 1.0 \pm 0.2$, $K_2^{34} = 1.0 \pm 0.1$, and $K_{int}^{34} = 1.3 \pm 0.3$, consistent with those obtained from analyzing the Gaussian-resolved E_{FRET} distribution (Figure 2D).

In the presence of excess unlabeled Hah1, the three E_{FRET} states were still observed for Cy3Cy5−MBD34^{L34}, shown by the 2-D E_{FRET} analysis (Figure S4B [SI]) and the E_{FRET} distribution (Figure 2E). Therefore, the two intramolecular−interdomain complexes of MBD34 still occur in the presence of Hah1. However, the apparent stabilities of these three states have changed, reflected by the changes in the peak area ratios in the E_{FRET} distribution (Figure 2G), and thus have the average dwell times of these three states (Table 1). These changes indicate that Hah1 interacts with MBD34 regardless of its two domains being in the extended conformation or forming intramolecular−interdomain complexes. Particularly, the ability of Hah1 to interact with the intramolecular−interdomain complexes of MBD34 indicates that Hah1, MBD3, and MBD4 can come together to form 3-body interactions, consistent with the population overlap between the complexes observed in the Cy5−Hah1 + Cy3−MBD34^{L4} and Cy5−Hah1 + Cy3−MBD34^{L3} experiments (section 3.3).

3.6. Cu$^+$-Dependence of Hah1−MBD34 Interactions. We further investigated the Cu$^+$-dependence of Hah1−MBD34 interactions using the Cy5−Hah1 + Cy3−MBD34^{L4} labeling scheme, which directly probes Hah1−MBD4 interactions. Cu$^+$-transfer can only occur between Hah1 and MBD4 here because the CXXC Cu$^+$-binding motif of MBD3 was mutated to AXXA. The Cu$^+$-dependence of the isolated Hah1−MBD3 interactions should be minimal, as Hah1 has merely small conformational changes upon Cu$^+$-binding.[27]

Three apparent E_{FRET} states (E^{L4}_{Low}, E^{L4}_{Mid}, and E^{L4}_{High}) are still observed in the presence of 1, 2, and 4 equiv of Cu$^+$ (Figure S4A [SI]). Again, the apparent E^{L4}_{Low} state contains contributions from the dissociated state, E_{Dissoc}, and Hah1 interactions with the unlabeled MBD3, E'^{L4}_{Low}. All three E_{FRET} values are similar to those in the absence of Cu$^+$ (Figure 1C), indicating that within our experimental limit the Hah1−MBD4 interaction geometries remain largely unchanged by Cu$^+$.

Yet, the stabilities and dynamics of the Hah1−MBD4 interactions are dependent on the presence of Cu$^+$, as shown by the Gaussian-resolved E_{FRET} distributions and average lifetimes (Figure 4). In the presence of 1 equiv of Cu$^+$, the E^{L4}_{Mid}/E_{Dissoc} and E^{L4}_{High}/E_{Dissoc} area ratios in the E_{FRET} distribution and the lifetimes of E^{L4}_{Mid} and E^{L4}_{High} do not change much compared with those of the *apo* protein interactions (Figure 4D, E). Therefore, Hah1 interactions with MBD4 are apparently unperturbed by 1 equiv of Cu$^+$. This is in contrast to the Cu$^+$-dependence of Hah1−MBD4^{SD} interactions, which showed a factor of ~1.3 stabilization at 1 equiv of Cu$^+$; this stabilization was attributable to Cu$^+$-bridging at the protein interaction interface.[2a,c,d,11,26c] This contrast indicates that the Cu$^+$-bridging-induced stabilization is insignificant for Hah1 interacting with the multidomain MBD34 construct, possibly because the *apo* Hah1−MBD4 interactions are already ~16 times more stable than the *apo* Hah1−MBD4^{SD} (Figure 2F). An NMR characterization of Hah1's interactions with a WDP multidomain construct containing MBDs 4−6 also showed that Cu$^+$ does not greatly perturb Hah1−MBD interactions.[14b]

In the presence of 2 equiv of Cu$^+$, the E^{L4}_{Mid}/E_{Dissoc} and E^{L4}_{High}/E_{Dissoc} area ratios both decrease by a factor of ~2 compared with the *apo* and 1 equiv Cu$^+$ conditions (Figure 4D). This decrease in stability can be attributed to a decrease in the average lifetimes of the E^{L4}_{Mid} and E^{L4}_{High} states, $\bar{\tau}_{Mid}$ and $\bar{\tau}_{High}$, which also decrease by a factor of ~2 (Figure 4E). No further change was observed in the E_{FRET} distribution (Figure 4C, D) or average lifetimes (Figure 4E) with 4 equiv Cu$^+$, indicating that both proteins are fully metalated at 2 equiv of Cu$^+$.

dx.doi.org/10.1021/ja3018835 | J. Am. Chem. Soc. 2012, 134, 8934−8943

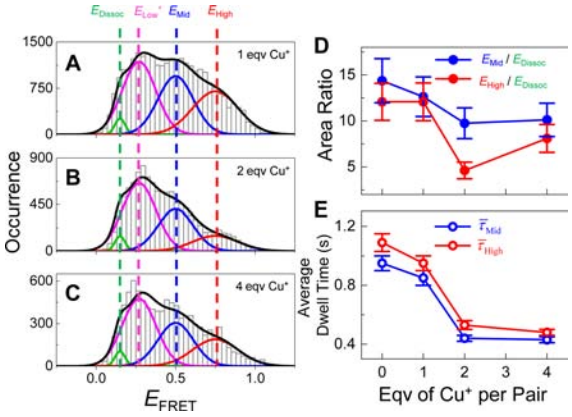

Figure 4. Compiled E_{FRET} distributions (bin size = 0.03) and Gaussian fits for Cy5−Hah1 + Cy3−MBD34^{L4} in the presence of (A) 1 equiv, (B) 2 equiv, and (C) 4 equiv of Cu^+ per protein pair. The E_{FRET} distributions were fitted globally with those in Figure 2 by sharing the center values and widths of each E_{FRET} state. The area ratio between E'^{L4}_{Low} and E^{L4}_{Dissoc} was kept constant using the approximation that the isolated Hah1−MBD3 interactions (represented by E'^{L4}_{Low}) should be largely independent of Cu^+. (D) Area ratios of E^{L4}_{Mid} and E^{L4}_{High} with respect to E^{L4}_{Dissoc} for Cy5−Hah1 + Cy3−MBD34^{L4} with varying equivalents of Cu^+. (E) Average dwell times of E^{L4}_{Mid} and E^{L4}_{High}, $\overline{\tau}_{Mid}$ and $\overline{\tau}_{High}$ respectively, for Cy5−Hah1 + Cy3−MBD34^{L4} with varying equivalents of Cu^+.

The observed destabilization of the Hah1−MBD4 interactions at excess Cu^+ relative to the *apo* condition was not observed in the Hah1−MBD4^{SD} interactions.[26c] Therefore, the destabilization must be associated with the multidomain nature of MBD34 compared with the isolated MBD4^{SD}. It is possible that the full metalation disrupts the concerted actions between the two domains of MBD34, that were facilitating interactions with Hah1.

4. DISCUSSION

We have used smFRET measurements combined with vesicle trapping to probe the weak and dynamic interactions between Hah1 and the double-domain MBD34 construct of WDP. By placing the FRET donor or acceptor on Hah1, MBD3, or MBD4 (section 3.1), we have examined how Hah1 interacts with MBD3 and MBD4 and how MBD3 and MBD4 interact with each other at the single-molecule level. For all cases, we observed two major interaction complexes that interconvert dynamically (section 3.2). The similarity in E_{FRET} values across all labeling schemes indicates that Hah1−MBD4, Hah1−MBD3, and MBD3−MBD4 interaction geometries are conserved, attributable to the sequence and structural homology among Hah1, MBD3, and MBD4.

The Hah1 interactions with MBD3 and MBD4 of MBD34 have similar stabilities (section 3.3). The Hah1−MBD4 interactions are significantly more stable than the Hah1−MBD4^{SD} interactions; this enhanced stability is associated with an increase in the protein association rate, not a decrease in the dissociation rates (section 3.4). An overlap population exists between Hah1−MBD3 and Hah1−MBD4 complexes, attributable to Hah1 interacting with MBD3 and MBD4 *simultaneously*, forming 3-body interactions. These 3-body interactions were further supported by intramolecular−interdomain MBD3−MBD4 complexes interacting with Hah1 (section 3.5).

In the presence of Cu^+ and regardless of Cu^+ stoichiometry, the Hah1−MBD4 interaction geometries appear unchanged, although the stabilities and lifetimes of the interaction complexes decreased under excess Cu^+ (section 3.6). This decrease in stability may be due to a disruption of concerted interactions within the double-domain MBD34, as this trend was not observed for Hah1−MBD4^{SD} interactions.

On the basis of the above results, we propose structural models for Hah1−MBD34 interactions. These models are then used to formulate a qualitative Hah1−MBD34 interaction mechanism that includes both 2-body and 3-body interactions between Hah1, MBD3, and MBD4.

4.1. Possible Structural Models of 2-Body and 3-Body Protein Interaction Complexes. Two major interaction geometries, E_{Mid} and E_{High}, were observed for Hah1−MBD4, Hah1−MBD3, and MBD3−MBD4 interactions. To better understand how Hah1 and MBD34 interact, here we propose *possible* structural models of interaction complexes based on our smFRET results and past structural studies of these or homologous proteins.

Hah1 and all WDP/MNK MBDs share the same $\beta\alpha\beta\beta\alpha\beta$ protein fold, and all contain the CXXC motif. The two α-helices are on one side of the protein (i.e., the "face" side), and the four β-strands form a β-sheet on the other side (i.e., the "back" side); we denote the "face" side of the protein with a green helix and the "back" side with a purple arrow in our cartoon representations in Figure 5.

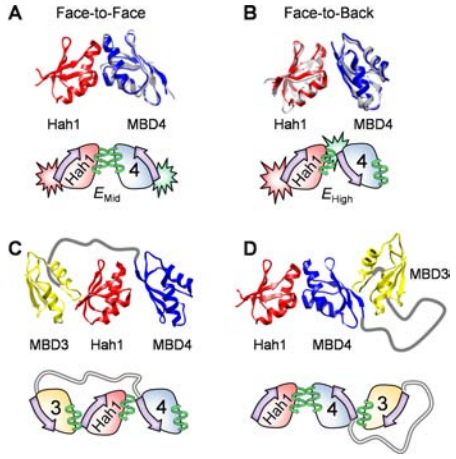

Figure 5. Structural models (top) of face-to-face (A) and face-to-back (B) Hah1−MBD4 interaction complexes with corresponding cartoon representations (bottom). Structural model of a 3-body interaction where Hah1 is sandwiched between MBD3 and MBD4 (C) and where Hah1 is interacting with an MBD34 intramolecular−interdomain adduct (D). In the cartoons, the "face" side of a protein is represented by a helix, and the "back" side is represented by an arrow. All models were generated by overlaying MBD3 (PDB code 2ROP, yellow) and/or MBD4 (PDB code 2ROP, blue) onto the Hah1−MNK1 structure (PDB code 2K1R, gray) for face-to-face interactions or onto the Hma7 dimer structure (PDB code 3DXS, gray) for the face-to-back interactions.

In our previous study of Hah1−MBD4^{SD} interactions,[26c] we have proposed a structural model giving rise to the E_{Mid} state based on an interaction geometry between Hah1 and the first N-terminal MBD of MNK, MNK1, observed by NMR (Figure 5A).[21e] In this geometry, Hah1 and the MBD interact in a face-to-face manner: their CXXC motifs face each other, where a metal ion can coordinate to cysteines from both proteins, thus

dx.doi.org/10.1021/ja3018835 | J. Am. Chem. Soc. 2012, 134, 8934−8943

Scheme 2. Illustrations of Major Features of Hah1−MBD34 Interaction Dynamics; (A, B) Intermolecular and Intramolecular Hah1−MBD4, Hah1−MBD3, and MBD3−MBD4 Interactions Can Occur in Two Major Geometries, Providing Versatile Docking with Interconversion for Cu^+ Transfer; (C) Hah1 Can Interact with Intramolecular−Interdomain MBD34 Complexes Linking MBD−MBD and Hah1−MBD Interactions; (D) 3-Body Interaction Where Hah1 Is Sandwiched Provides a Mechanism to Reroute Hah1 between MBDs

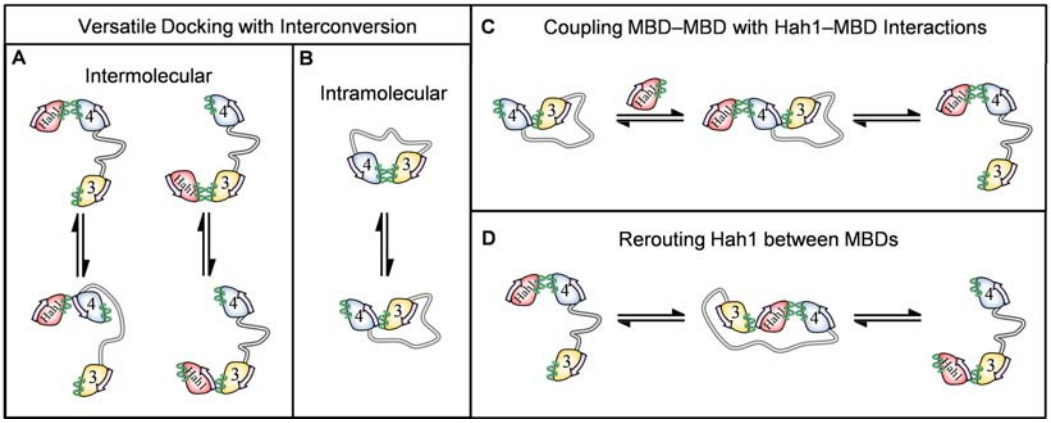

offering a facile pathway for metal transfer via ligand exchange.[2a,c,d,11a−c]

For the E_{High} state, we propose a preliminary structural model based on the crystal structure of an asymmetric dimer of the MBD of Hma7, a Cu^+-transporting ATPase in *Arabidopsis thaliana*; this MBD is homologous to Hah1 and WDP/MNK MBDs.[22b] In this Hma7MBD dimer, the face side of one monomer interacts with the back side of the other monomer (Figure 5B); we refer to this interaction geometry as face-to-back.

To generate the face-to-face and face-to-back structural models, we overlaid the known structures of Hah1, MBD3, and MBD4 onto the experimental Hah1−MNK1 and Hma7MBD dimer structures (section S14 [SI]). A and B of Figure 5 illustrate the Hah1−MBD4 face-to-face and face-to-back interaction models, respectively. The corresponding FRET donor−acceptor distances in the face-to-face models are longer than those in the face-to-back models, consistent with $E_{Mid} < E_{High}$. All these models also have thermodynamic stability comparable to the experimental Hah1-MNK1 and Hma7 dimer structures based on detailed interface thermodynamic analyses (sections S14−S15 [SI]) and molecular dynamics simulations (sections S16−S17 [SI]).

The face and back interfaces are spatially distinct (i.e., nonoverlapping), making it possible for 3-body interactions between Hah1, MBD3, and MBD4; we thus generated models for 3-body interactions using combinations of face-to-face and face-to-back interactions (section S18 [SI]). C and D of Figure 5 illustrate two possible 3-body interactions: in one Hah1 is sandwiched between MBD3 and MBD4 (Figure 5C), and in the other Hah1 interacts with an intramolecular MBD3−MBD4 complex (Figure 5D). These 3-body interaction models can account for our observed population overlap between Hah1−MBD3 and Hah1−MBD4 complexes (section 3.3) and the perturbation in intramolecular−interdomain MBD3−MBD4 interactions in the presence of Hah1 (section 3.5).

We emphasize that the interaction geometries here are only proposed models that are supported by data and deduced from known structures of protein complexes (sections S14−S18 [SI]). Within either E_{Mid} or E_{High} states, additional subpopulations could exist that are unresolved in our measurements. The dynamic linker between MBD4 and MBD3 may also play a role in the complex formation.[12d]

4.2. Hah1−MBD34 Interaction Mechanism and Its Functional Implications. Using the proposed interaction models, Scheme 2 illustrates the major features of dynamic Hah1−MBD34 interactions, which were observed experimentally: (1) intermolecular interactions of Hah1 with MBD4 or MBD3, each forming two interaction geometries that interconvert dynamically (Scheme 2A), (2) intramolecular interactions between MBD4 and MBD3, forming two interconverting interaction geometries (Scheme 2B), and (3) formation of 3-body interactions between Hah1, MBD4, and MBD3 (Scheme 2C, D). A more detailed mechanistic model and accompanying analysis are presented in sections S19−S21 (SI) for further discussion.

Inside cells Hah1 delivers Cu^+ to WDP (or MNK), which translocates Cu^+ across membranes for either incorporation to downstream copper proteins or efflux. WDP must operate with both efficiency and versatility to receive, reroute, and export the Cu^+ delivery from many Hah1 molecules. Considering that WDP has six MBDs, the major features of the Hah1−MBD34 interactions are advantageous for fulfilling these functions.

The operation versatility of WDP can be accomplished by providing multiple MBDs for Hah1 to dock and deliver its cargo. Hah1 can dock at each MBD with two different geometries (Scheme 2A) and can further interconvert between its docking geometries dynamically, thus allowing either of the two interfaces to be exposed for interaction with an additional MBD. The 3-body interactions where Hah1 is sandwiched between MBDs allow for the rerouting of Cu^+ delivery, i.e., a Hah1 molecule can be handed over directly from one MBD to another (Scheme 2C). This rerouting of Hah1 would especially be useful when the initially targeted MBD is already loaded with Cu^+. Consistent with this scenario, a decrease in complex stability and lifetime was observed when Hah1 and MBD34 are fully metalated (section 3.6), facilitating the departure of Hah1.

WDP's intramolecular MBD−MBD interactions provide a way for internal redistribution of Cu^+ (Scheme 2B), either to vacate space for next Hah1 delivery or to traffic Cu^+ downstream. This redistribution also occurs in a versatile manner, as multiple binding geometries were observed between MBD3 and MBD4. This internal Cu^+ redistribution among

dx.doi.org/10.1021/ja3018835 | J. Am. Chem. Soc. 2012, 134, 8934−8943

MBDs can be directly coupled to the Cu^+ delivery or export through Hah1 interactions with the intramolecular MBD−MBD complexes (Scheme 2D).

All of these processes occur on similar time scales (~1 s), including the protein associations at the effective μM concentration inside vesicles. (Note the intracellular concentration of the yeast Hah1 homologue Atx1 is also about μM.[28]) Their similarity in time scale suggests that all these processes should occur comparably inside cells for function.

Our proposed Hah1−MBD34 interaction mechanism may also help understand the regulatory function of the MBDs, where Hah1−MBD or MBD−MBD interactions modulate the ATPase activity associated with Cu^+-translocation[4c,7,17] or the kinase-mediated phosphorylation associated with the relocalization of WDP/MNK for Cu^+-efflux.[4c,16,18] It was proposed that large-scale conformational changes within the N-terminal tail of WDP/MNK act as the regulatory switch,[12a,d,14a,19] which disrupts MBD interactions with the catalytic core affecting Cu^+-translocation or exposes/hides phosphorylation sites in the linker regions. The 3-body interactions where Hah1 is sandwiched between MBDs (Scheme 2D) could induce large-scale conformational changes in the cytoplasmic tail of WDP, and hence, may play a role in this regulatory switching mechanism.

■ ASSOCIATED CONTENT

Supporting Information

Detailed experimental methods. Empirical calibration curve for apparent E_{FRET} vs donor−acceptor anchor-to-anchor distance. Determination of intramolecular MBD3−MBD4 interaction rate constants. Additional two-dimensional E_{FRET} histogram analysis. Interface analysis and molecular dynamics simulations for 2-body interaction models. Potential 3-body interaction complexes. Putative Hah1−MBD34 interaction mechanism with discussions on the relation of E_{FRET} observables to chemical species and thermodynamic quantifications. This material is available free of charge via the Internet at http://pubs.acs.org.

■ AUTHOR INFORMATION

Corresponding Author

pc252@cornell.edu

Present Addresses

[§]David Geffen School of Medicine, University of California, Los Angeles, CA 90095.

[⊥]Department of Chemistry, University of North Carolina, Chapel Hill, NC 27599.

Notes

The authors declare no competing financial interest.

■ ACKNOWLEDGMENTS

We thank Amy Rosenzweig and Liliya Yatsunyk for providing plasmids, Cynthia Kinsland for performing part of the mutagenesis, University Michigan Mass Spectrometry Facility for protein mass analyses, Francesca Cantini for providing the full MBD34 NMR structure containing the linker region, and Debashis Panda for preparing the apparent E_{FRET} vs probe anchor-to-anchor distance calibration curve. This work was supported mainly by NIH (R01 GM082939) with partial support by NSF (CHE-0645392, for developing the vesicle trapping combined with smFRET approach), and a Sloan fellowship (P.C.). A.M.K. and J.J.B. had support from the NIH Molecular Biophysics Traineeship Grant (T32 GM008267-23).

■ REFERENCES

(1) (a) Kim, B.-E.; Nevitt, T.; Thiele, D. J. *Nat. Chem. Biol.* **2008**, *4*, 176. (b) Jomova, K.; Vondrakova, D.; Lawson, M.; Valko, M. K. *Mol. Cell. Biochem.* **2010**, *345*, 91. (c) Robinson, N. J.; Winge, D. R. *Annu. Rev. Biochem.* **2010**, *79*, 537.

(2) (a) Pufahl, R. A.; Singer, C. P.; Peariso, K. L.; Lin, S.-J.; Schmidt, P. J.; Fahrni, C. J.; Culotta, V. C.; Penner-Hahn, J. E.; O'Halloran, T. V. *Science* **1997**, *278*, 853. (b) Hamza, I.; Schaefer, M.; Klomp, L. W. J.; Gitlin, J. D. *Proc. Natl. Acad. Sci. U.S.A.* **1999**, *96*, 13363. (c) Larin, D.; Mekios, C.; Das, K.; Ross, B.; Yang, A.-S.; Gilliam, T. C. *J. Biol. Chem.* **1999**, *274*, 28497. (d) O'Halloran, T. V.; Culotta, V. C. *J. Biol. Chem.* **2000**, *275*, 25057.

(3) (a) Terada, K.; Nakako, T.; Yang, X. L.; Iida, M.; Aiba, N.; Minamiya, Y.; Nakai, M.; Sakaki, T.; Miura, N.; Sugiyama, T. *J. Biol. Chem.* **1998**, *273*, 1815. (b) Petris, M. J.; Strausak, D.; Mercer, J. F. *Hum. Mol. Genet.* **2000**, *9*, 2845.

(4) (a) Hung, I. H.; Suzuki, M.; Yamaguchi, Y.; Yuan, D. S.; Klausner, R. D.; Gitlin, J. D. *J. Biol. Chem.* **1997**, *272*, 21461. (b) Petris, M. J.; Mercer, J. F.; Culvenor, J. G.; Lockhart, P.; Gleeson, P. A.; Camakaris, J. *EMBO J.* **1996**, *15*, 6084. (c) Lutsenko, S.; LeShane, E. S.; Shinde, U. *Arch. Biochem. Biophys.* **2007**, *463*, 134.

(5) (a) Wilson, S. A. K. *Brain* **1912**, *34*, 296. (b) Menkes, J. H.; Alter, M.; Steigleder, G. K.; Weakley, D. R.; Sung, J. H. *Pediatrics* **1962**, *29*, 764. (c) Mercer, J. F. B. *Trends Mol. Med.* **2001**, *7*, 64. (d) Lutsenko, S.; Barnes, N. L.; Bartee, M. Y.; Dmitriev, O. Y. *Physiol. Rev.* **2007**, *87*, 1011.

(6) Arguello, J. M. *J. Membr. Biol.* **2003**, *195*, 93.

(7) Arguello, J. M.; Eren, E.; Gonzalez-Guerrero, M. *Biometals* **2007**, *20*, 233.

(8) Boal, A. K.; Rosenzweig, A. C. *Chem. Rev.* **2009**, *109*, 4760.

(9) (a) Yatsunyk, L. A.; Rosenzweig, A. C. *J. Biol. Chem.* **2007**, *282*, 8622. (b) Banci, L.; Bertini, I.; Ciofi-Baffoni, S.; Kozyreva, T.; Zovo, K.; Palumaa, P. *Nature* **2010**, *465*, 645. (c) Xiao, Z.; Loughlin, F.; George, G. N.; Howlett, G. J.; Wedd, A. G. *J. Am. Chem. Soc.* **2004**, *126*, 3081. (d) Xiao, Z.; Wedd, A. G. *Nat. Prod. Rep.* **2010**, *27*, 768. (e) Xiao, Z.; Brose, J.; Schimo, S.; Ackland, S. M.; La Fontaine, S.; Wedd, A. G. *J. Biol. Chem.* **2011**, *286*, 11047. (f) Badarau, A.; Dennison, C. *J. Am. Chem. Soc.* **2011**, *133*, 2983. (g) Badarau, A.; Dennison, C. *Proc. Natl. Acad. Sci. U.S.A.* **2011**, *108*, 13007.

(10) Banci, L.; Bertini, I.; Cantini, F.; Massagni, C.; Migliardi, M.; Rosato, A. *J. Biol. Chem.* **2009**, *284*, 9354.

(11) (a) Wernimont, A. K.; Huffman, D. L.; Lamb, A. L.; O'Halloran, T. V.; Rosenzweig, A. C. *Nat. Struct. Biol.* **2000**, *7*, 766. (b) Arnesano, F.; Banci, L.; Bertini, I.; Bonvin, M. J. J. *Structure* **2004**, *12*, 669. (c) Huffman, D. L.; O'Halloran, T. V. *Annu. Rev. Biochem.* **2001**, *70*, 677. (d) Rodriguez-Granillo, A.; Crespo, A.; Estrin, D. A.; Wittung-Stafshede, P. *J. Phys. Chem. B* **2010**, *114*, 3698.

(12) (a) Walker, J. M.; Huster, D.; Ralle, M.; Morgan, C. T.; Blackburn, N. J.; Lutsenko, S. *J. Biol. Chem.* **2004**, *279*, 15376. (b) Achila, D.; Banci, L.; Bertini, I.; Bunce, J.; Ciofi-Baffoni, S.; Huffman, D. L. *Proc. Natl. Acad. Sci. U.S.A.* **2006**, *103*, 5729. (c) Rodriguez-Granillo, A.; Crespo, A.; Wittung-Stafshede, P. *Biochemistry* **2009**, *48*, 5849. (d) Rodriguez-Granillo, A.; Crespo, A.; Wittung-Stafshede, P. *J. Phys. Chem. B* **2010**, *114*, 1836.

(13) van Dongen, E. M.; Klomp, L. W.; Merkx, M. *Biochem. Biophys. Res. Commun.* **2004**, *323*, 789.

(14) (a) Banci, L.; Bertini, I.; Cantini, F.; Della-Malva, N.; Migliardi, M.; Rosato, A. *J. Biol. Chem.* **2007**, *282*, 23140. (b) Fatemi, N.; Korzhnev, D. M.; Velyvis, A.; Sarkar, B.; Forman-Kay, J. D. *Biochemistry* **2010**, 8468.

(15) (a) Iida, M.; Terada, K.; Sambongi, Y.; Wakabayashi, T.; Miura, N.; Koyama, K.; Futai, M.; Sugiyama, T. *FEBS Lett.* **1998**, *428*, 281. (b) Forbes, J. R.; Hsi, G.; Cox, D. W. *J. Biol. Chem.* **1999**, *274*, 12408.

(16) Cater, M. A.; Forbes, J.; La Fontaine, S.; Cox, D.; Mercer, J. F. *Biochem. J.* **2004**, *380*, 805.

(17) (a) Gonzalez-Guerrero, M.; Arguello, J. M. *Proc. Natl. Acad. Sci. U.S.A.* **2008**, *105*, 5992. (b) Wu, C. C.; Rice, W. J.; Stokes, D. L. *Structure* **2008**, *16*, 976. (c) Gourdon, P.; Liu, X. Y.; Skjorringe, T.; Morth, J. P.; Moller, L. B.; Pedersen, B. P.; Nissen, P. *Nature* **2011**, *475*, 59.

(18) (a) Vanderwerf, S. M.; Cooper, M. J.; Stetsenko, I. V.; Lutsenko, S. *J. Biol. Chem.* **2001**, *276*, 36289. (b) Bartee, M. Y.; Ralle, M.; Lutsenko, S. *Biochemistry* **2009**, *48*, 5573. (c) Pilankatta, R.; Lewis, D.; Adams, C. M.; Inesi, G. *J. Biol. Chem.* **2009**, *284*, 21307. (d) Veldhuis, N. A.; Valova, V. A.; Gaeth, A. P.; Palstra, N.; Hannan, K. M.; Michell, B. J.; Kelly, L. E.; Jennings, I.; Kemp, B. E.; Pearson, R. B.; Robinson, P. J.; Camakaris, J. *Int. J. Biochem. Cell Biol.* **2009**, *41*, 2403. (e) Pilankatta, R.; Lewis, D.; Inesi, G. *J. Biol. Chem.* **2011**, *286*, 7389.

(19) (a) Leshane, E. S.; Shinde, U.; Walker, J. M.; Barry, A. N.; Blackburn, N. J.; Ralle, M.; Lutsenko, S. *J. Biol. Chem.* **2010**, *285*, 6327. (b) Tsivkovskii, R.; MacArthur, B. C.; Lutsenko, S. *J. Biol. Chem.* **2001**, *276*, 2234. (c) DiDonato, M.; Hsu, H. F.; Narindrasorasak, S.; Que, L., Jr.; Sarkar, B. *Biochemistry* **2000**, *39*, 1890.

(20) (a) Multhaup, G.; Strausak, D.; Bissig, K.-D.; Solioz, M. *Biochem. Biophys. Res. Commun.* **2001**, *288*, 172. (b) Strausak, D.; Howies, M. K.; Firth, S. D.; Schlicksupp, A.; Pipkorn, R.; Multhaup, G.; Mercer, J. F. B. *J. Biol. Chem.* **2003**, *278*, 20821.

(21) (a) Arnesano, F.; Banci, L.; Bertini, I.; Cantini, F.; Ciofi-Baffoni, S.; Huffman, D. L.; O'Halloran, T. V. *J. Biol. Chem.* **2001**, *276*, 41365. (b) Banci, L.; Bertini, I.; Cantini, F.; Felli, I. C.; Gonnelli, L.; Hadjiliadis, N.; Pierattelli, R.; Rosato, A.; Voulgaris, P. *Nat. Chem. Biol.* **2006**, *2*, 367. (c) Banci, L.; Bertini, I.; Cantini, F.; Chasapis, C. T.; Hadjiliadis, N.; Rosato, A. *J. Biol. Chem.* **2005**, *280*, 38259. (d) Banci, L.; Bertini, I.; Francesca, C.; Rosenzweig, A. C.; Yatsunyk, L. A. *Biochemistry* **2008**, *47*, 7423. (e) Banci, L.; Bertini, I.; Calderone, V.; Della-Malva, N.; Felli, I. C.; Neri, S.; Pavelkova, A.; Rosato, A. *Biochem. J.* **2009**, *422*, 37.

(22) (a) Badarau, A.; Firbank, S. J.; McCarthy, A. A.; Banfield, M. J.; Dennison, C. *Biochemistry* **2010**, 7798. (b) Zimmerman, M.; Clarke, O.; Gulbis, J. M.; Keizer, D. W.; Jarvis, R. S.; Cobbett, C. S.; Hinds, M. G.; Xiao, Z.; Wedd, A. G. *Biochemistry* **2009**, 11640. (c) Alvarez, H. M.; Xue, Y.; Robinson, C. D.; Canalizo-Hernández, M. A.; Marvin, R. G.; Kelly, R. A.; Mondragón, A.; Penner-Hahn, J. E.; O'Halloran, T. V. *Science* **2009**, *327*, 331.

(23) Hussain, F.; Rodriguez-Granillo, A.; Wittung-Stafshede, P. *J. Am. Chem. Soc.* **2009**, *131*, 16371.

(24) Ha, T. *Methods* **2001**, *25*, 78.

(25) (a) Chiu, D. T.; Wilson, C. F.; Karlsson, A.; Danielsson, A.; Lundqvist, A.; Strömberg, A.; Ryttsén, F.; Davidson, M.; Nordholm, S.; Orwar, O.; Zare, R. N. *Chem. Phys.* **1999**, *247*, 133. (b) Boukobza, E.; Sonnenfeld, A.; Haran, G. *J. Phys. Chem. B.* **2001**, *105*, 12165. (c) Okumus, B.; Wilson, T. J.; Lilley, D. M. J.; Ha, T. *Biophys. J.* **2004**, *87*, 2798. (d) Benitez, J. J.; Keller, A. M.; Chen, P. *Methods Enzymol.* **2010**, *472*, 41.

(26) (a) Benitez, J. J.; Keller, A. M.; Ochieng, P.; Yatsunyk, L. A.; Huffman, D. L.; Rosenzweig, A. C.; Chen, P. *J. Am. Chem. Soc.* **2008**, *130*, 2446. (b) Benitez, J. J.; Keller, A. M.; Ochieng, P.; Yatsunyk, L. A.; Huffman, D. L.; Rosenzweig, A. C.; Chen, P. *J. Am. Chem. Soc.* **2009**, *131*, 871. (c) Benitez, J. J.; Keller, A. M.; Huffman, D. L.; Yatsunyk, L.; Rosenzweig, A. C.; Chen, P. *Faraday Discuss.* **2011**, *148*, 71.

(27) Anastassopoulou, I.; Banci, L.; Bertini, I.; Cantini, F.; Katsari, E.; Rosato, A. *Biochemistry* **2004**, *43*, 13046.

(28) Portnoy, M. E.; Rosenzweig, A. C.; Rae, T. D.; Huffman, D. L.; O'Halloran, T. V.; Culotta, V. C. *J. Biol. Chem.* **1999**, *274*, 15041.